



ELSEVIER

Contents lists available at [SciVerse ScienceDirect](http://www.sciencedirect.com)

Chemical Engineering Science

journal homepage: www.elsevier.com/locate/ces

Gas–liquid two-phase flow in microchannel at elevated pressure

Yuchao Zhao, Guangwen Chen*, Chunbo Ye, Quan Yuan

Dalian National Laboratory for Clean Energy, Dalian Institute of Chemical Physics, Chinese Academy of Sciences, Dalian 116023, China

HIGHLIGHTS

- ▶ Seven typical flow patterns are observed at T-junction microchannel.
- ▶ Detail characteristics of flow patterns at different pressure are investigated.
- ▶ Formation mechanism and process of observed flow patterns are discussed.
- ▶ Flow pattern maps are divided into five regions based on the formation mechanism.
- ▶ Transition lines shift to higher We_{GS} and lower We_{LS} at elevated pressure.

ARTICLE INFO

Article history:

Received 24 January 2012

Received in revised form

28 September 2012

Accepted 6 October 2012

Available online 22 October 2012

Keywords:

Microreactor

Microstructure

Multiphase flow

Hydrodynamics

Mixing

High pressure

ABSTRACT

The present study deals with pressure effects on the hydrodynamic characteristics of gas–liquid two phases within a T-junction microchannel. The operating pressure is in the range of 0.1~5.0 MPa. Nitrogen and de-ionized water are selected as the test fluids. The gas Weber numbers vary from 1.37×10^{-5} to 3.46 at atmospheric pressure and from 1.70×10^{-3} to 70.32 at elevated pressure, respectively. The liquid Weber numbers are in the range of 3.1×10^{-3} ~4.9. The operating pressure plays an important role in gas–liquid two phases flow. Seven typical flow patterns such as bubbly flow, slug flow, unstable slug flow, parallel flow, slug-annular flow, annular flow, and churn flow are observed. Based on the force analysis of the gas and liquid phase in microchannel, the formation mechanisms of flow patterns are discussed at great length, and the flow pattern maps are divided into five regions using We_{GS} and We_{LS} as coordinates. These results are beneficial for future investigation to understand gas–liquid two-phase mass transfer and reaction characteristics in microchannel at elevated pressure.

© 2012 Elsevier Ltd. All rights reserved.

1. Introduction

The characteristics of chemical engineering in microscale have been developing very fast within the last decade (Jähnisch et al., 2004; Kockmann, 2007; Zhao et al., 2006). Their extremely large surface-to-volume ratio and the short transport path in microchannels can enhance heat and mass transfer dramatically, which make them ideal candidates for heat exchangers and microreactors. In addition, scale-up is achieved by simple replication of microreactor units. The numbering-up mode can eliminate costly reactor redesign and pilot plant experiments, and shorten the research and development time from lab to industrial production. All above advantages could provide many potential opportunities in chemical process intensification and miniaturization development, especially for multiphase systems, such as gas–liquid,

liquid–liquid, gas–liquid–solid, etc. (Abdallah et al., 2004; Chen et al., 2011; Kashid et al., 2011; Zhao et al., 2007).

The hydrodynamic characteristics of multiphase flow play an important role in the design and numbering-up of microreactor. Obviously, for gas–liquid and gas–liquid–solid systems, a good understanding of gas–liquid two-phase flow and mass transfer in microchannels is beneficial to further analyzing multiphase reaction processes. A great number of studies for investigating the gas–liquid flow in microchannels have been carried out at atmospheric conditions. Five main flow patterns such as bubble, slug or Taylor, slug-annular, annular, and churn have been observed depending on the liquid properties, channel diameter, operating conditions, and inlet geometry (Kawahara et al., 2002; Triplett et al., 1999; Waelchli and Rohr, 2006; Yue et al., 2007, 2008, 2009). Flow pattern maps for gas–liquid flow in microchannel are plotted based on the superficial velocities of gas and liquid phase (Coleman and Garimella, 1999; Kawahara et al., 2002; Triplett et al., 1999; Zhao and Bi, 2001).

The majority of gas–liquid reaction processes occurring in microreactors, such as hydrogenation (Halder and Lawal, 2007;

* Corresponding author. Tel.: +86 411 84379031; fax: +86 411 84691570.
E-mail address: gwchen@dicp.ac.cn (G. Chen).

Tadepalli et al., 2007; Yeong et al., 2004), oxidation (Leclerc et al., 2008), Fischer–Tropsch synthesis (Deshmukh et al., 2010), carbonylation and hydroformylation (Mills and Chaudhari, 1997) and CO₂ absorption (Ye et al., 2012), etc., are generally performed at 1–10 MPa in order to improve reaction performance, increase the solubility of gaseous reactant, and achieve high transport efficiency. Unfortunately, there was no guarantee that the information available for the atmospheric cases could be extrapolated to the elevated pressure situations, even little attention had been paid to the gas–liquid two-phase flow in microchannels at elevated pressure. Trachsel et al. (2008) validated slug flow by laser-induced fluorescence (LIF) using Rhodamine B as fluorochrome at ambient temperature and pressures ranging from 5 to 50 bar. There was lack of a comprehensive and systematic understanding of other gas–liquid two-phase flow patterns at elevated pressure. In fact, the difference between the atmospheric pressure and the elevated pressure is mainly induced by the increase of the gas density, which is realized by increasing molecular numbers in unit volume. The gas density could also be modified by other methods. For example, Stanley et al. (1997) used argon, helium and nitrogen gas to vary the gas density, but their investigations were mainly focused on two-phase heat transfer. The ultimate aims of our entire research program are to investigate the characteristics of the gas–liquid two-phase flow, mass transfer, and reaction at elevated pressure in the microreactor. Some specific transport and reaction phenomena are expected to be found due to the increase of the operating pressure. The relevant investigations are focused on the variation of the operating pressure.

In the present work, the main objective is to experimentally study the gas–liquid two-phase flow patterns in the T-junction rectangular microchannel with the hydraulic diameter of 0.4 mm. De-ionized water and nitrogen are used as the working fluids. Flow patterns are identified by examining the images recorded using a CCD camera.

2. Experimental section

As shown in Fig. 1, the inlet configuration of the microreactor is T-shaped opposed junction. The microreactor includes the top/bottom housing sections with an open space for visual observation at elevated pressure, which are made of stainless steel plate; and the top/bottom covers with T-junction microchannel, which are fabricated on the polymethyl methacrylate substrate (PMMA, A grade, 92% of light transmittance, ShenZhen HuiLi Acrylic

Products Co., Ltd) using micromachining technology (FANUC KPC-30a) in our CNC Machining Center. The cross section of all channels is 300 μm (depth) × 600 μm (width), with the hydraulic diameter of 400 μm. The length of mixing channel is 60 mm. The surface roughness after machining is ± 2.5 μm. In order to seal the T-junction microchannel, the top housing section, the top cover, the bottom cover, and the bottom housing section are orderly placed from up to down, then clamped through nuts and bolts. The sealing performance is confirmed at 7.0 MPa by gas-tightness test.

The schematic of the experimental setup is shown in Fig. 2. The working fluids are nitrogen and de-ionized water. The de-ionized water is first boiled in a beaker to fully remove the dissolved gases (~0.2–0.5 μS/cm). A high precision digital piston pump is used to convey de-ionized water into one inlet of the horizontal T-shaped rectangular microchannel (Series II, Chrom. Tech. Inc.). The liquid flow rate is calibrated by the weighing method with an accuracy of ± 0.001 g, and the resulting accuracy of the flow rate is ± 0.002 mL/min. The flow damper, liquid storage tank, and one-way valve are used in series to damp possible flow pulsations. Nitrogen is led into another inlet of the T-shaped microchannel from a gas cylinder. The flow rates are precisely controlled by the mass flow controllers with different flow ranges. At last, the gas–liquid two-phase mixture flows into a gas–liquid separator at the end of the system, the gas and liquid

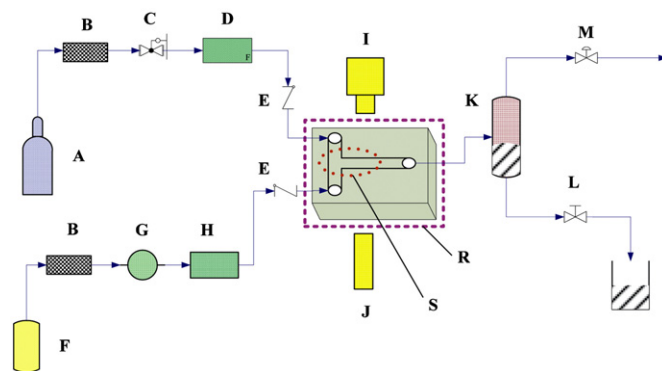


Fig. 2. Schematic of the experimental setup for gas–liquid two-phase system at elevated pressure. (A), N₂ Cylinder; (B), filter; (C), pressure relief valve; (D), mass flow controller; (E), one-way valve; (F), water tank; (G), Series II digital pump; (H), liquid damper; (I), CCD high-speed camera; (J), illumination system; (K), gas–liquid separator; (L) high pressure stop valve; (M), back pressure regulating valve; (R) T-shaped microchannel; and (S), shooting zone.

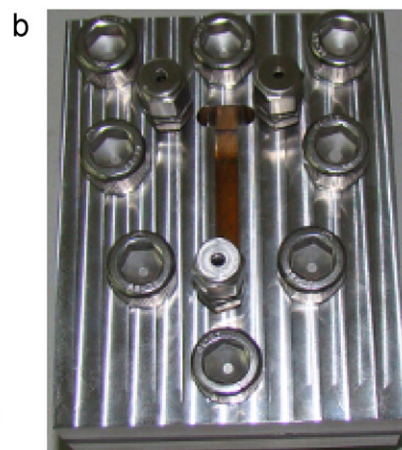
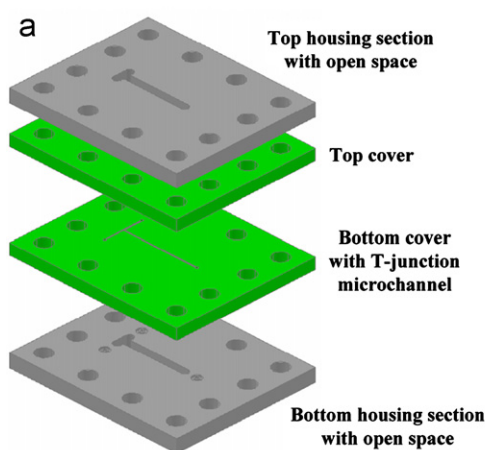


Fig. 1. Components of T-junction microchannel for gas–liquid two-phase system at elevated pressure. (a) Construction of T-junction microchannel, and (b) actual picture of T-junction microchannel.

are discharged from the top of the back pressure regulating valve and the bottom of the high pressure stop valve, respectively. During experimental processes, the operating pressure in micro-reactor is regulated by the pressure relief valve and the back pressure regulating valve. Three thermocouples (K-type) are located in the two inlets and the outlet to measure the corresponding temperatures. All experiments are maintained between 19 °C and 21 °C.

The flow patterns in the T-junction microchannel are recorded by a CCD high-speed camera system (BASLER A504kc), with a recording speed of 1000 frames per second. The shooting zone is set at the T-junction and in the downstream channel after the T-junction. The shooting length is about 15 mm. The light beam used for the visualization is provided through an adjustable light source under the test section. Every run must be repeated at least twice to ensure the reproducibility of experimental data.

3. Results and discussion

3.1. Physical properties of fluids and definition of parameters

The system pressures are varied in the range of 0.1~5.0 MPa in our experiments. The solubility of nitrogen in water is only about 0.685 cm³/g at 20 °C and 5.0 MPa (Baranenko et al., 1990). The volume of maximum dissolved gas accounts for only 1.4 vol% of total gas volume, and therefore the decrease of the gas volume

can be ignored. According to the ideal gas equation, gas density increases almost proportionally to pressure, as shown in Eq. (1)

$$\rho_r = \frac{P_r}{P_a} \cdot \rho_a \quad (1)$$

Wiegand and Franck (1994) measured experimentally the interfacial tension of N₂-Water system at high pressures by the method of the Pendant Drop. The interfacial tension of N₂-Water system in this paper can be deduced from their results, as shown in Table 1. It can be seen that the operating pressure has a little effect on the interfacial tension of gas-liquid two phases. The effects of pressure on the liquid density and the viscosity of gas-liquid two phases can also be ignored.

The superficial velocity of nitrogen and water can be calculated by the following equations:

$$j_{GS} = \frac{Q_G}{A} \cdot \frac{P_a}{P_r} \quad (2)$$

$$j_{LS} = \frac{Q_L}{A} \quad (3)$$

The Weber numbers of nitrogen and water are calculated in terms of the superficial velocities, as follows:

$$We_{GS} = \frac{D_H \cdot j_{GS}^2 \cdot \rho_r}{\sigma} \quad (4)$$

$$We_{LS} = \frac{D_H \cdot j_{LS}^2 \cdot \rho_L}{\sigma} \quad (5)$$

In our experiments, the gas and liquid superficial velocities are in the range of $4.62 \times 10^{-2} \sim 23.15$ m/s and $2.31 \times 10^{-2} \sim 0.93$ m/s, respectively. The gas Weber numbers vary from 1.37×10^{-5} to 3.46 at atmospheric pressure and from 1.70×10^{-3} to 70.32 at elevated pressure, respectively. The liquid Weber numbers are in the range of $3.1 \times 10^{-3} \sim 4.9$. The effect of operating pressure on the liquid Weber numbers can almost be ignored.

Table 1
Physical Properties of N₂-Water system (293.15 K).

Pressure/MPa	0.1	1.0	2.0	3.0	4.0	5.0
Density/kg m ⁻³	1.16	11.64	23.28	34.92	46.56	58.20
Interfacial tension/mN m ⁻¹	72.10	71.43	70.96	70.45	69.82	69.23

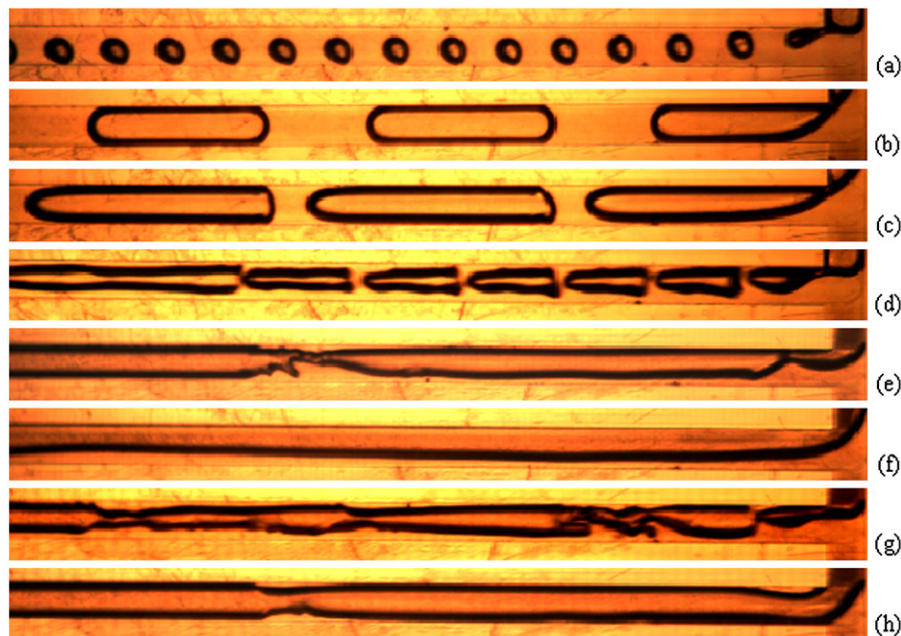


Fig. 3. Representative photographs of flow patterns in the T-junction microchannel at atmospheric pressure (flow direction is from right to left, the shooting zone is at the T-junction and its downstream 8 mm of microchannel). (a) Bubbly flow ($j_{GS}=0.28$ m/s, $We_{GS}=4.92 \times 10^{-4}$; $j_{LS}=0.74$ m/s, $We_{LS}=3.04$). (b) Slug flow ($j_{GS}=0.18$ m/s, $We_{GS}=2.19 \times 10^{-4}$; $j_{LS}=9.26 \times 10^{-2}$ m/s, $We_{LS}=4.76 \times 10^{-2}$). (c) Slug flow ($j_{GS}=0.93$ m/s, $We_{GS}=5.47 \times 10^{-3}$; $j_{LS}=0.19$ m/s, $We_{LS}=0.20$). (d) Unstable slug flow ($j_{GS}=1.85$ m/s, $We_{GS}=2.19 \times 10^{-2}$; $j_{LS}=0.74$ m/s, $We_{LS}=3.04$). (e) Slug-annular flow ($j_{GS}=3.70$ m/s, $We_{GS}=8.86 \times 10^{-2}$; $j_{LS}=0.19$ m/s, $We_{LS}=0.20$). (f) Parallel flow ($j_{GS}=3.70$ m/s, $We_{GS}=8.86 \times 10^{-2}$; $j_{LS}=2.31 \times 10^{-2}$ m/s, $We_{LS}=2.97 \times 10^{-3}$). (g) Churn flow ($j_{GS}=9.26$ m/s, $We_{GS}=0.55$; $j_{LS}=0.74$ m/s, $We_{LS}=3.04$). (h) Annular flow ($j_{GS}=23.15$ m/s, $We_{GS}=3.46$; $j_{LS}=0.093$ m/s, $We_{LS}=0.048$).

3.2. Two-phase flow patterns at different pressures

Figs. 3 and 4 show typical images of two-phase flow patterns in the T-junction microchannel at atmospheric and 5.0 MPa pressure, respectively. Seven distinct flow patterns, that is, bubbly flow, slug flow, unstable slug flow, slug-annular flow, parallel flow, annular flow, and churn flow, are observed and categorized in accordance with the flow patterns defined by Kawahara et al. (2002), Shao et al. (2009), Triplett et al. (1999), and Yue et al. (2008).

Bubbly flow is observed at relatively lower gas velocity (or We_{GS}) and higher liquid velocity (or We_{LS}), as shown in Figs. 3(a) and 4(a). The near-spherical or spherical bubbles, which are uniform in size, are dispersed in the liquid and their diameters are all smaller than the microchannel width. The distance between two consecutive gas bubbles is nearly equal and coalescence is hardly observed during our experiments. The shape and size of bubbles in microchannel are mainly determined by operating conditions, inlet mixing zone configuration (Shao et al., 2011; Qian and Lawal, 2006; Yue et al., 2008; Garstecki et al., 2006; Triplett et al., 1999; Coleman and Garimella, 1999), and flow pulsations of gas or liquid according to our experimental observations. The latter two cases are the key factors that lead to the occurrence of the non-uniformity and the coalescence of bubbles in microchannels. This can be avoided by well-defined inlet configuration and liquid damper in our experiments, as well as careful manipulating. From Figs. 3(a) and 4(a), we can see that the size of gas bubble decreases and the formation frequency of gas bubbles increases with the increase of operating pressure at the same real gas and liquid velocity. This is of great benefit to the increase of gas–liquid mass transfer performance.

The length of gas bubbles longer than the width of micro-channel is a feature of slug flow, as shown in Figs. 3(b),(c) and 4(b),(c). This flow pattern generally appears at low j_{GS} ($0.046 \text{ m/s} < j_{GS} < 1.39 \text{ m/s}$) and j_{LS} ($0.093 \text{ m/s} < j_{LS} < 0.74 \text{ m/s}$). At extremely low We_{GS} and We_{LS} , the nose and the tail of gas slug preserve nice symmetry, and appear to have near-hemispheric shape. Although the nose of gas slug becomes thin and sharp with the increase of We_{GS} and We_{LS} , the tail of gas slug turns to be more flattened, as shown in Figs. 3(c) and 4(c). Likewise, there is no coalescence of two consecutive gas slugs. From Figs. 3(b),(c) and 4(b),(c), we can also see that, with the increase of operating pressure at given gas and liquid velocity, the size of gas slug decreases and the formation frequency of gas slug increases. Moreover, with the increase of pressure, the formation location of gas slug moves to downstream of the T-junction along the main channel.

With a further increase of the gas flow rate, unstable slug flow starts to occur, as shown in Figs. 3(d) and 4(d). It can also be considered as one sub-regime of slug flow, as well as the description of Yue et al. (2008). The size and shape of gas slug exhibit intense randomness. The coalescence and rupture of gas slug become frequent, especially for those elevated pressure situations. The unstable gas slugs are generally formed at the T-junction of microchannel at atmospheric pressure. However, at elevated pressure, it occurs at the downstream of the T-junction along the main channel.

With the increase of We_{GS} in unstable slug flow at relatively low We_{LS} , all liquid bridges between two consecutive gas slugs are penetrated by gas flow, which are simultaneously accompanied by the appearance of some sparse thin gas necks with a deformed liquid film, this is called slug-annular flow. Moreover, the number

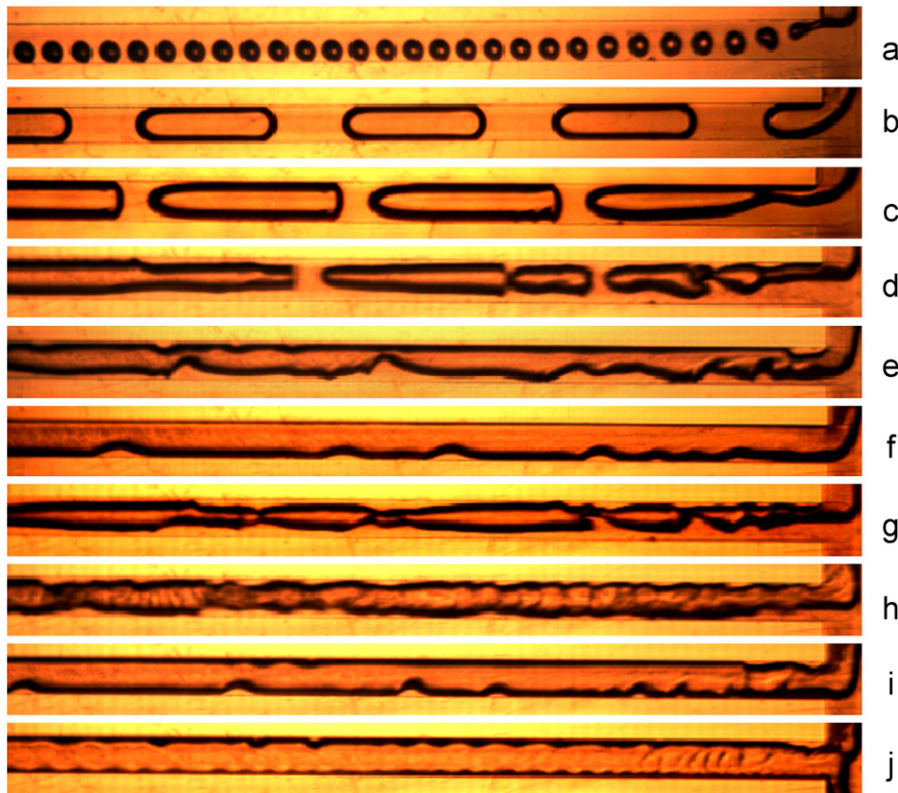


Fig. 4. Representative photographs of flow patterns in the T-junction microchannel at 5.0 MPa pressure (flow direction is from right to left, the shooting zone is at the T-junction and its downstream 8 mm of microchannel). (a) Bubbly flow ($j_{GS}=0.28 \text{ m/s}$, $We_{GS}=2.59 \times 10^{-2}$; $j_{LS}=0.74 \text{ m/s}$, $We_{LS}=3.17$). (b) Slug flow ($j_{GS}=0.18 \text{ m/s}$, $We_{GS}=1.15 \times 10^{-2}$; $j_{LS}=9.26 \times 10^{-2} \text{ m/s}$, $We_{LS}=4.95 \times 10^{-2}$). (c) Slug flow ($j_{GS}=0.93 \text{ m/s}$, $We_{GS}=0.29$; $j_{LS}=0.19 \text{ m/s}$, $We_{LS}=0.20$). (d) Unstable slug flow ($j_{GS}=1.85 \text{ m/s}$, $We_{GS}=1.15$; $j_{LS}=0.74 \text{ m/s}$, $We_{LS}=3.17$). (e) Slug-annular flow ($j_{GS}=3.70 \text{ m/s}$, $We_{GS}=4.61$; $j_{LS}=0.19 \text{ m/s}$, $We_{LS}=0.20$). (f) Parallel flow ($j_{GS}=3.70 \text{ m/s}$, $We_{GS}=4.61$; $j_{LS}=2.31 \times 10^{-2} \text{ m/s}$, $We_{LS}=3.10 \times 10^{-3}$). (g) Churn flow ($j_{GS}=2.78 \text{ m/s}$, $We_{GS}=2.59$; $j_{LS}=0.74 \text{ m/s}$, $We_{LS}=3.17$). (h) Churn flow ($j_{GS}=9.26 \text{ m/s}$, $We_{GS}=28.83$; $j_{LS}=0.74 \text{ m/s}$, $We_{LS}=3.17$). (i) Annular flow ($j_{GS}=5.56 \text{ m/s}$, $We_{GS}=10.38$; $j_{LS}=4.63 \times 10^{-2} \text{ m/s}$, $We_{LS}=1.24 \times 10^{-2}$). (j) Annular flow ($j_{GS}=9.26 \text{ m/s}$, $We_{GS}=28.83$; $j_{LS}=4.63 \times 10^{-2} \text{ m/s}$, $We_{LS}=1.24 \times 10^{-2}$).

of thin gas neck and the liquid film thickness increase with the increase of operating pressure, as shown in Figs. 3(e) and 4(e).

When the gas–liquid two phases are completely separated and flow side by side in microchannel at extremely low liquid and medium gas velocity, the parallel flow forms as shown in Figs. 3(f) and 4(f). The similar flow pattern was also observed by Kawahara et al. (2011). This is different from the conventional stratified flow in large pipes where gas–liquid two phases separate up and down due to gravity. In addition, we can also see the interface of the gas–liquid two phases appears as smooth and wavy at atmospheric and elevated pressure, respectively.

Only one type of churn flow in our experiments is found at atmospheric pressure. However, both types of churn flow appear at elevated pressure, as shown in Figs. 3(g) and 4(g),(h). We also find the highly irregular gas–liquid interface and the serpentine-like gas core with a deformed liquid film. The formation frequency and the amplitude solitary waves of thin gas neck are higher compared to slug-annular flow. At elevated pressure, the width of gas neck increases and finally approaches to the width of microchannel with the increase of We_{GS} and We_{LS} , as shown in Fig. 4(h). Meanwhile, the surface of gas core shows quasi-spiral striations and the interface of gas–liquid two phases becomes extremely unstable, which produces tremendous gas–liquid interfacial area as well as the interfacial surface renewal velocity. These flow characteristics are all beneficial to gas–liquid two-phase mass transfer performance.

Increasing We_{GS} with lower We_{LS} at slug-annular flow or parallel flow leads to the formation of annular flow, which is characterized by the flowing of the thin liquid film on the microchannel wall and gas phase in the microchannel core, as shown in Figs. 3(h) and 4(i),(j). Only one type of annular flow is observed at atmospheric pressure, however, both types of annular flow can be formed at elevated pressure in our experiments. It can be seen that the thickness of liquid film at elevated pressure is smaller than at atmospheric pressure by comparing Figs. 3(h) and 4(i),(j). At atmospheric pressure, the annular flow is comparatively stable and the interface fluctuation of gas–liquid two phases cannot be found, but a single thin gas neck occasionally appears. At elevated pressure, the oscillation of the interface of gas–liquid two phases is formed, and the amplitude and frequency of the fluctuation increase with the increase of gas velocity.

3.3. Formation mechanism of flow patterns

The formation of different flow patterns is mainly dependent on the competition of the interfacial tension and the inertia force for multiphase system, which is represented by the dimensionless number We_{GS} and We_{LS} . The dispersion of gas phase and two-phase flow characteristics present in T-junction microchannel are

considered to be mainly governed by three kinds of force. The liquid inertia force is in favor of deforming and breaking up the gas phase. The gas inertia force tends to make the gas phase continuous and occupy larger space in the channel. The interfacial tension of gas–liquid two phases is beneficial to stabilize the dispersing gas phase. In addition, the existence of liquid films and the fluid-wall contact dynamics can also be affected by the surface properties of microchannel (Cubaud et al., 2006).

3.4. Bubbly flow formed in dripping regime

Fig. 5(a)–(b) shows the typical photographs of bubbly flow formation process at atmospheric and 5.0 MPa pressure, respectively. Its formation mechanism can be subordinated to the dripping regime according to the description of some investigators (Fu et al., 2010; de Menech et al., 2008) and is similar to “flow focusing” mode (Anna et al., 2003; Ganán-Calvo and Gordillo, 2001). The formation of gas bubble in the dripping regime takes place by two steps: (1) the growth of gas bubble at the T-junction, and (2) the necking and detaching. After the bubble detaching, the newly built end of the thin gas neck recoils, and the quasi-spindle-shaped gas bubble relaxes back to the near-spherical shape. The diameter of gas bubble quickly decreases with the increase of liquid flow rates at a given gas flow rate. The gas bubble size slightly increases with the increase of gas flow rates at a given liquid flow rate.

In this flow pattern, the liquid inertia force, rather than the interfacial tension and the gas inertia force, dominates the formation of gas bubble in microchannel with the lower We_{GS} and higher We_{LS} . Therefore, the gas phase can be easily dispersed by the liquid phase. The gas bubbles volume is determined by the liquid inertia force, and the diameter is mainly influenced by the liquid flow rates. In considering the dispersed gas bubbles, their shape is controlled by the interfacial tension more than the gas inertia force, so the shape of gas bubbles remains near-spherical. The flow characteristics of liquid phase are also affected by the liquid inertia force. The advancing contact angle and the receding contact angle can be considered as 180° and 0° under these operating conditions, respectively. As a result, the liquid phase can spread completely over the channel wall. Elevated pressure changes the behavior of the two-phase flow and the way they physically interact, which is attributed to the increase of the gas density. At given gas and liquid velocity, the stability of the gas–liquid interface decreases with increase of pressure (Letzel et al., 1999), and this will be more favorable for producing smaller gas bubbles under the liquid inertia force dominating zone. The interfacial tension varies from 72.10 mN m^{-1} to 69.23 mN m^{-1} when the operating pressure is increased from 0.1 MPa to 5.0 MPa. The decrease in the interfacial tension reduces gas

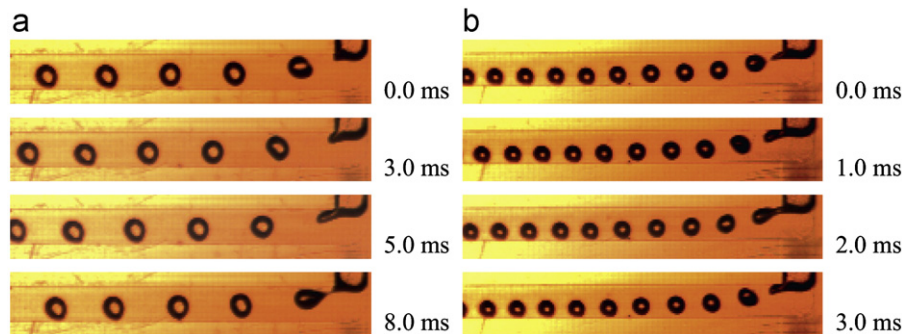


Fig. 5. Typical photographs of bubbly flow formation process (a) atmospheric and (b) 5.0 MPa pressure. (a) $j_{GS}=0.19 \text{ m/s}$, $We_{GS}=2.19 \times 10^{-4}$; $j_{LS}=0.74 \text{ m/s}$, $We_{LS}=3.04$. (b) $j_{GS}=0.19 \text{ m/s}$, $We_{GS}=1.15 \times 10^{-2}$; $j_{LS}=0.74 \text{ m/s}$, $We_{LS}=3.17$.

bubble size and benefits the formation frequency of gas bubbles (Xu et al., 2006).

3.5. Slug flow formed in squeezing regime

Fig. 6(a)–(b) shows the time evolution of a periodic break-up procedure for slug flow formation process at atmospheric and 5.0 MPa pressure, respectively. The formation of gas slug in different inlet configurations has been studied by many investigators (Garstecki et al., 2006; Kreutzer et al., 2005; Qian and Lawal, 2006; Shao et al., 2011). It can be described by the squeezing mechanism and divided into three steps. Firstly, the gas phase expands from the T-junction to the downstream until the gas slug nose blocks the entire main channel. The expansion of gas slug is mainly induced by the upstream pressure of gas phase and the neck gradually comes into being at the T-junction. Secondly, the gas slug nose continues to move down the stream along the main microchannel accompanied with the increase of gas slug length. Simultaneously, the neck width slowly decreases until it finally breaks up, then one gas bubble forms in the main microchannel. After the break-up of gas slug, the gas slug rear quickly shrinks nearly hemispherical tip and a new process repeats. The gas slugs can be generated uniformly over a wide range of gas and liquid flow rates, moreover, the length of gas slugs predominantly depends on the variation of the gas and liquid flow rates.

The gas–liquid impinging interaction is weaker at the T-junction due to the lower gas and liquid superficial velocity, and the liquid inertia force is not a key factor for break-up of the gas phase. A high pressure zone will form near the channel wall opposite to the inlet of main channel during the gas–liquid two-phase fluids interacting according to Garstecki et al. (2006). The gas phase penetrates into the main channel, at the same time, a neck connecting the quasi-gas slug and the bulk gas phase forms at the downstream edge of the inlet under the pressure gradient. The interfacial tension, rather than the liquid inertia force and the gas inertia force, dominates the formation of gas bubbles in microchannel with extremely low We_{GS} and We_{LS} . The nose and tail of the dispersed gas remain regularly near-hemispherical configuration. Both the advancing contact angle and the receding contact angle can be considered as approaching its static contact

angle (ca. 70°), that is, the liquid phase exists as regularly intermittent liquid slugs and can spread partially over the channel wall, as shown in Fig. 6. The gas inertia force increases at higher We_{GS} , which results in an increase of the length of gas slugs. At given gas and liquid velocity, the stability of the gas–liquid interface decreases with the increase of pressure, this will be favor of producing smaller gas slugs and increasing the formation frequency of gas slugs under the interfacial tension dominating zone at elevated pressure. The formation location of gas slug moves to downstream of the T-junction, as shown in Figs. 3(c) and 4(c). This can be explained from the lower liquid inertia force and the weaker gas–liquid interface interaction.

3.6. Unstable slug flow formed in randomness regime

Fig. 7(a)–(b) shows the random formation process of unstable slug flow during 3 ms at atmospheric and 5.0 MPa pressure, respectively. The formation of unstable gas slugs can be considered as a random regime and divided into three steps: (1) the gas neck, which connects the quasi-breaking up unstable gas slug and the bulk gas phase, penetrates into the liquid phase in the main channel and acts as the gas transmission channel; (2) the quasi-breaking up unstable gas slug elongates and expands by gas transmission in the neck, simultaneously, some gas nodes form in the main channel; and (3) the gas nodes break up randomly.

Although j_{GS} or We_{GS} increases, to some extent, and the gas inertia force begins to work compared with the slug flow, the interfacial tension still plays an important role in the shape of gas phase. Thus, the interface of gas–liquid two phases is difficult to remain regularly in a fixed shape. The gas slugs different in size are formed in the main channel. Simultaneously, the coalescence and rupture of adjacent gas slugs occur frequently. At given gas velocity, the neck, as well as the unstable gas slugs, becomes thinner and shorter with the increase of liquid velocity. There is also an increase of the coalescence and rupture frequency of adjacent gas slugs. In addition, both the nose and tail of gas slugs tend to sharpen, and the quasi-spindle-shaped gas slugs are formed. This is caused by the increase of the liquid inertia force and the interface interaction. From Fig. 7(a)–(b), we can also see that the neck is thicker and longer at elevated pressure than that at atmosphere pressure. Some shorter gas slugs and unstable gas

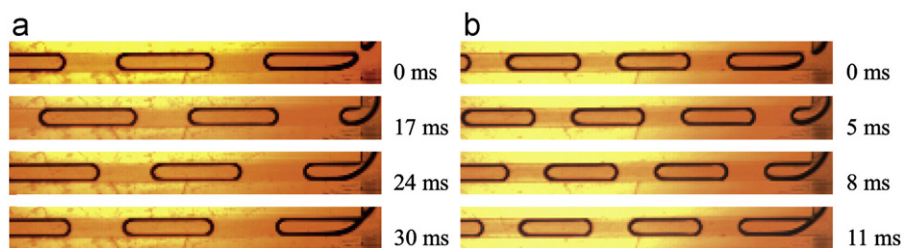


Fig. 6. Typical photographs of slug flow formation process (a) atmospheric and (b) 5.0 MPa pressure. (a) $j_{GS}=0.19$ m/s, $We_{GS}=2.19 \times 10^{-4}$; $j_{LS}=9.26 \times 10^{-2}$ m/s, $We_{LS}=4.76 \times 10^{-2}$. (b) $j_{GS}=0.19$ m/s, $We_{GS}=1.15 \times 10^{-2}$; $j_{LS}=9.26 \times 10^{-2}$ m/s, $We_{LS}=4.95 \times 10^{-2}$.

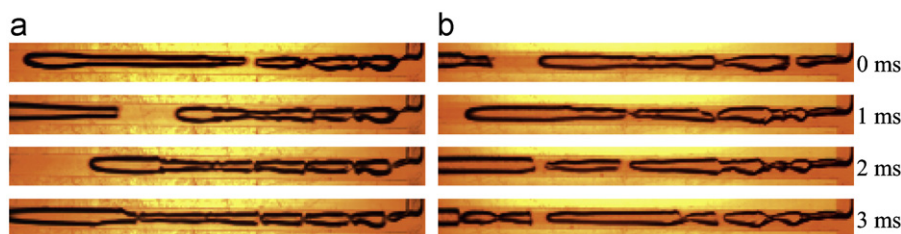


Fig. 7. Typical photographs of unstable slug flow formation process (a) atmospheric and (b) 5.0 MPa pressure. (a) $j_{GS}=1.85$ m/s, $We_{GS}=2.19 \times 10^{-2}$; $j_{LS}=0.74$ m/s, $We_{LS}=3.04$. (b) $j_{GS}=1.85$ m/s, $We_{GS}=1.15$; $j_{LS}=0.74$ m/s, $We_{LS}=3.17$.

slugs with the higher formation frequency are all found in our experiments. At given gas and liquid velocity, the stability of the gas–liquid interface will decrease with increasing pressure and gas inertia force. This will be favor of producing shorter gas slugs and increasing the formation frequency of unstable gas slugs where the interfacial tension and the gas inertia force commonly dominate. In addition, the inhibition effect on the break-up of the gas transmission neck begins to emerge at the T-junction due to the increase of the gas inertia force.

3.7. Slug-annular and parallel flow formed in continuous regime

Fig. 8(a)–(b) shows the formation process for slug-annular flow during 3 ms at atmospheric pressure and 5.0 MPa pressure, respectively. The formation of slug-annular flow can be considered as a continuous regime and generally occurs at medium gas and liquid velocity zone. The flow characteristics of gas–liquid two phases are commonly affected by the interfacial tension, the gas inertia force and the liquid inertia force. Although the gas phase cannot be broken up by the liquid phase at the T-junction or in the main channel due to the lower liquid inertia force, the liquid phase can still arrive at the opposite channel wall and form the liquid film. The interfacial tension plays a more important role in the liquid phase status than the liquid inertia force. Since the advancing contact angle and the receding contact angle tend to approach the static contact angle (ca. 70°), the gas nodes and the irregular interfacial waves are formed. The kinetic energy and momentum of the gas phase increase with the increase of the gas phase density, which leads to the increase of the collision energy at the gas–liquid two-phase interface. Thus, the number of gas

nodes, the frequency and amplitude of waves markedly increase with the increase of the operating pressure.

The parallel flow is formed at high gas and extremely low liquid velocity zone, and its formation mechanism can also be considered as the continuous regime. Fig. 9 shows that the liquid phase cannot penetrate into the gas phase and is completely limited to one side of channel by gas phase. This is caused by the high gas inertia force and the extremely low liquid inertia force. The increase of We_{GS} or the gas inertia force with increasing operating pressure makes the impinging intensity of gas–liquid two phases increase at given gas and liquid velocity, and the wavy interface phenomenon appears, as shown in Fig. 9(b).

3.8. Annular flow formed in engulfment regime

Annular flow generally occurs at higher We_{GS} and lower We_{LS} , and its formation can be considered as the engulfment regime, as shown in Fig. 10. The liquid inertia force is much lower than the gas inertia force, and therefore the liquid phase cannot enter the main channel by penetrating or squeezing and is limited in its inlet channel by gas phase, which results in the increase of local pressure at the liquid phase inlet. Eventually, the liquid phase is engulfed into the main channel in the form of ultra-thin liquid film by the gas phase with higher kinetic energy. Moreover, the liquid film thickness decreases and the intensity of engulfment increases with the increase of operating pressure, as shown in Fig. 10. The annular flow is comparatively stable and the interface fluctuation could not be found at atmospheric pressure, but a single thin gas neck occasionally appears. At elevated pressure, the oscillation of the interface of gas–liquid two phases is formed,

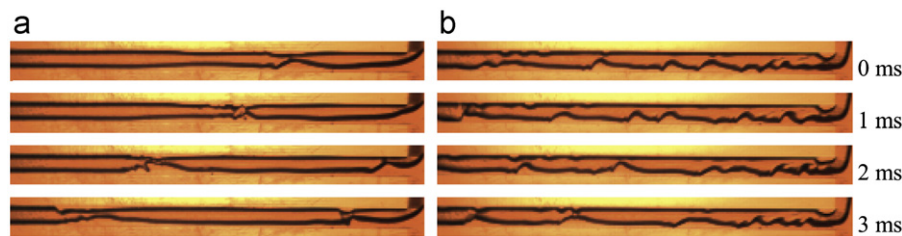


Fig. 8. Typical photographs of slug-annular flow formation process (a) atmospheric and (b) 5.0 MPa pressure. (a) $j_{GS}=3.70$ m/s, $We_{GS}=8.86 \times 10^{-2}$; $j_{LS}=0.19$ m/s, $We_{LS}=0.20$. (b) $j_{GS}=3.70$ m/s, $We_{GS}=4.61$; $j_{LS}=0.19$ m/s, $We_{LS}=0.20$.

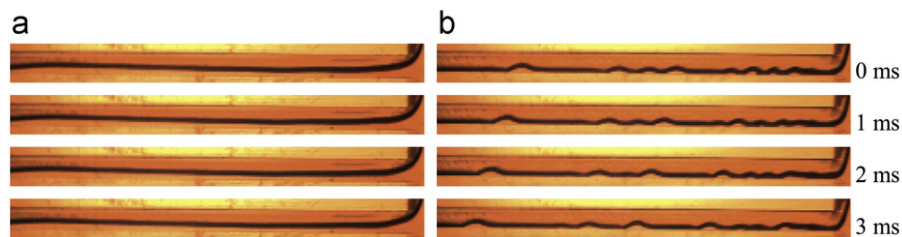


Fig. 9. Typical photographs of parallel flow formation process (a) atmospheric and (b) 5.0 MPa pressure. (a) $j_{GS}=3.70$ m/s, $We_{GS}=8.86 \times 10^{-2}$; $j_{LS}=2.31 \times 10^{-2}$ m/s, $We_{LS}=2.97 \times 10^{-3}$. (b) $j_{GS}=3.70$ m/s, $We_{GS}=4.61$; $j_{LS}=2.31 \times 10^{-2}$ m/s, $We_{LS}=3.10 \times 10^{-3}$.

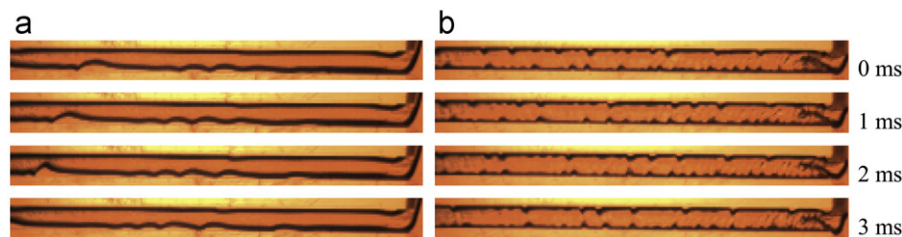


Fig. 10. Typical photographs of annular flow formation process (a) atmospheric and (b) 5.0 MPa pressure. (a) $j_{GS}=18.52$ m/s, $We_{GS}=2.22$; $j_{LS}=4.63 \times 10^{-2}$ m/s, $We_{LS}=1.19 \times 10^{-2}$. (b) $j_{GS}=9.26$ m/s, $We_{GS}=28.83$; $j_{LS}=9.26 \times 10^{-2}$ m/s, $We_{LS}=4.95 \times 10^{-2}$.

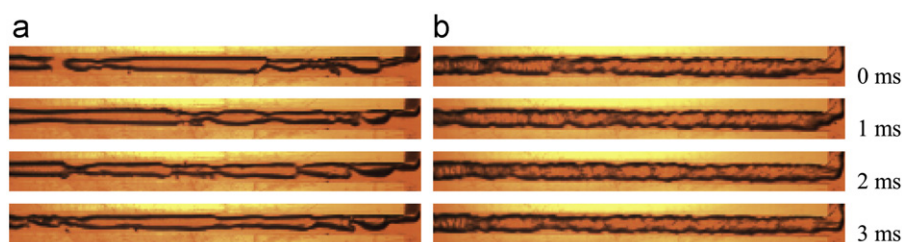


Fig. 11. Typical photographs of churn flow formation process (a) atmospheric and (b) 5.0 MPa pressure. (a) $j_{GS}=9.26$ m/s, $We_{GS}=0.55$; $j_{LS}=0.74$ m/s, $We_{LS}=3.04$. (b) $j_{GS}=9.26$ m/s, $We_{GS}=28.83$; $j_{LS}=0.74$ m/s, $We_{LS}=3.17$.

while the amplitude and frequency of the fluctuation increase with the increase of gas velocity. From Fig. 10(b), we can also see that there is a weakly quasi-spiral striations flow in the interface of gas–liquid two phases at the T-junction. The intensity of the quasi-spiral striation flow increases with increasing operating pressure and gas or liquid velocity due to the increase of the impinging intensity of gas–liquid two phases. The similarity in the same flow patterns, by comparing the atmospheric pressure with the elevated pressure, is lowered with increasing of the gas flow rates, as shown in Figs. 3–10. For example, the similarity in the slug flow in Fig. 6 is much larger than in the churn flow in Fig. 11 at different operating pressures. The effect of operating pressure on flow patterns at high gas flow rates are greater than that at low gas flow rates due to the higher kinetic energy and momentum. So the engulfment phenomenon occurs easily at the T-junction for annular flow at elevated pressure.

3.9. Churn flow formed in randomness or engulfment regime

Generally, the flow pattern is found at higher We_{GS} and We_{LS} , and it can be considered as one of the most important flow patterns for intensifying the gas–liquid two-phase mass transfer, in which the flow dynamics is very sensitive to the operating pressure. Its formation mechanism can be considered as the randomness regime at atmospheric pressure according to the characteristics of the formation process, and it turns into the engulfment regime with the increase of gas velocity at elevated pressure, as shown in Figs. 4 and 11. Although the flow characteristics of gas–liquid two phases are commonly determined by the gas inertia force and the liquid inertia force according to the values of We_{GS} and We_{LS} , the gas phase cannot be broken up by the liquid phase at the T-junction or in the main channel due to the extremely high gas inertia force. So the gas neck, acting as the gas transmission channel, forms and penetrates into the liquid phase in the main channel at atmospheric pressure. This is somewhat similar to the unstable slug flow. Some random gas nodes are also formed in the main channel under these situations. At given gas (or liquid) velocity, the gas neck gradually becomes thinner (or thicker) with the increase of liquid (or gas) velocity, while the frequency and amplitude of waves are markedly increased at the gas–liquid two-phase interface.

At elevated pressure, there is an intensively quasi-spiral striation flow in the gas–liquid two-phase interface at the T-junction and in the main channel. The intensity of the quasi-spiral spin increases dramatically with the operating pressure and gas or liquid velocity, as shown in Fig. 11(b). This behavior can be explained that the increase of the kinetic energy and momentum of the gas–liquid two phases leads to the increase of the collision energy at the gas–liquid two-phase interface. The degree of irregularity of the gas–liquid interface is increased significantly due to the increase of the gas inertia force at elevated pressure, which can produce larger gas–liquid interfacial area and intensify

the gas–liquid mass transfer performance compared to the atmospheric pressure.

3.10. Flow patterns map at atmospheric pressure and elevated pressure

Fig. 12(a)–(f) shows gas–liquid two-phase flow pattern maps in the T-junction microchannel at atmospheric pressure and elevated pressure as a function of the superficial gas and liquid velocities, respectively. The flow transition lines proposed by Triplett et al. (1999) for 1.097 mm diameter circular and 1.09 mm-hydraulic diameter semi-triangular microchannels are included for comparison. The transitions from unstable slug flow to slug-annular flow and churn flow can be well represented by Triplett's predictions at atmospheric pressure. Other transition lines are in poor agreement with the Triplett's model, and the difference is intensified with the increase of operating pressure, which is probably caused by the different experimental conditions, such as gas–liquid inlet configuration, channel geometry (cross-sectional shape) and material, etc. All transition lines seem to be shifted towards lower j_{GS} and j_{LS} with the increase of operating pressure. The regions of annular and churn flow become wider at elevated pressure than that at atmospheric pressure. However, the intrinsic reason for the transformation of the transition lines caused by the increase of operating pressure cannot be clearly represented in Fig. 12, and the formation mechanisms of flow patterns are not reflected in these flow pattern maps. Thus, the empirical correlations only based on j_{GS} and j_{LS} are unsuitable for interpreting the flow pattern transition behavior in the T-junction microchannel.

In accordance with the aforementioned discussion, the hydrodynamic characteristics of gas–liquid two phases are mainly affected by the interfacial tension of gas–liquid two phases, the gas inertia force and the liquid inertia force. The flow transition correlations based on Weber numbers, which correlate the interfacial tension and the inertia force, seem to be more reasonable for interpreting the flow pattern transition behavior in the T-junction microchannel. Akbar et al. (2003) divided the entire flow regime map into four regions (surface tension-dominated zone, transition zone, inertia-dominated zone 1 and inertia-dominated zone 2), and subsequently, Yue et al. (2008) proposed a transition line correlation from slug to unstable slug flow in Y-junction microchannel according to their experimental data. Fig. 13 compares our experimental data and the transition lines proposed by Akbar et al. (2003), and Yue et al. (2008) in the flow pattern maps using We_{GS} and We_{LS} as coordinates. Akbar's and Yue's models are not well to conform to our experimental results at atmospheric, as well as the elevated pressure, which is probably caused by the difference of channel inlet geometry. For Y-junction microchannel or other similar gas–liquid mixers, bubbly flow and slug flow are much easier to be formed due to the shear stresses. Churn flow zone becomes larger because of the intensive collision of the gas–liquid two phases at the T-junction. Based on the analysis for the formation mechanism and process of various flow patterns,

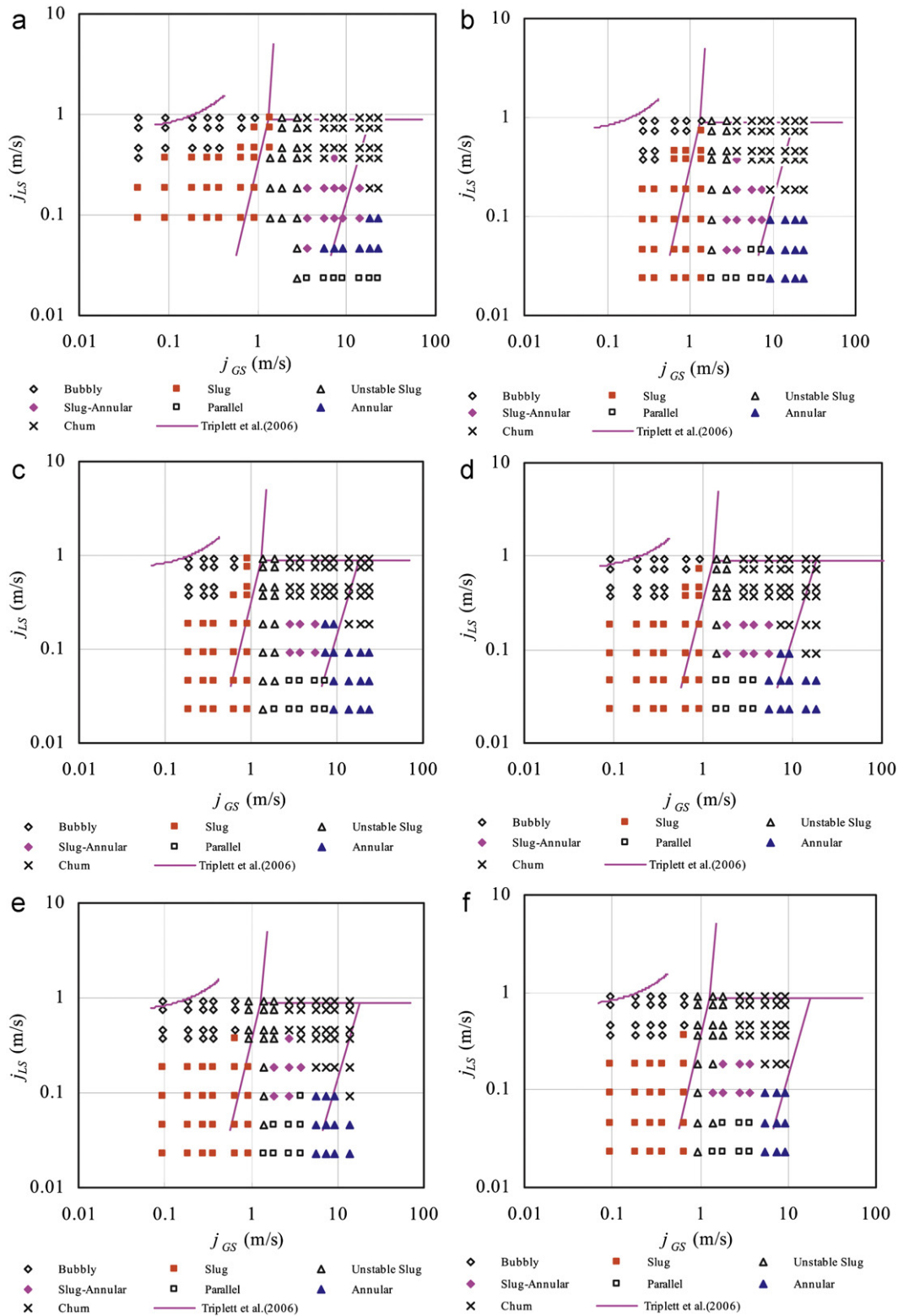


Fig. 12. Flow pattern maps for the present microchannel based on the superficial gas and liquid velocities.

the flow patterns map is divided into five regions using We_{GS} and We_{LS} as coordinates. As shown in Fig. 13:

(a) zone I: the interfacial tension and the inertia force of liquid phase dominate, mainly including bubbly flow, for

$We_{LS} \geq 0.94 \exp(118.48We_{GS})$ at atmospheric pressure and for $We_{LS} \geq (0.8-0.09P) \exp[(16.15-1.56P)We_{GS}]$ at elevated pressure ($1.0 \text{ MPa} \leq P \leq 5.0 \text{ MPa}$).

(b) zone II: the interfacial tension dominates, mainly including slug flow, for $We_{GS} \leq 0.012$ and $We_{LS} < 0.94 \exp(118.48We_{GS})$ at

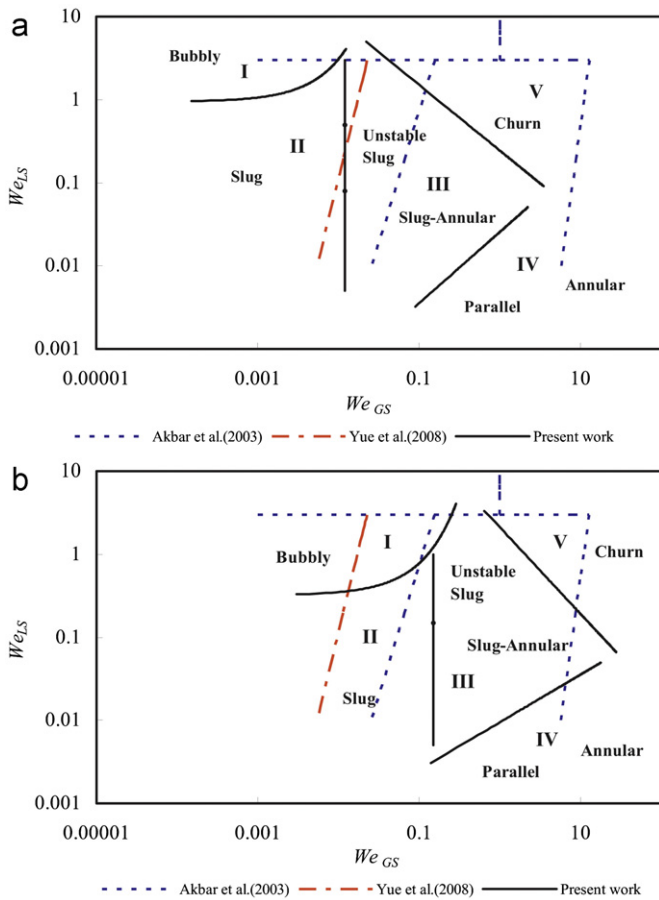


Fig. 13. Flow pattern maps for the present T-junction microchannel based on We_{GS} and We_{LS} .

atmospheric pressure; for $We_{GS} \leq 0.15$ and $We_{LS} < (0.8-0.09P) \exp[(16.15-1.56P)We_{GS}]$ at elevated pressure ($1.0 \text{ MPa} \leq P \leq 5.0 \text{ MPa}$).

- (c) zone III: the interfacial tension, the gas inertia force and the liquid inertia force commonly dominate, mainly including unstable slug flow and slug-annular flow, for $We_{GS} > 0.012$, $We_{LS} < 0.94 \exp(118.48We_{GS})$, $We_{LS} \leq 0.24We_{GS}^{-0.79}$ and $We_{LS} \geq 0.026We_{GS}^{0.86}$ at atmospheric pressure; for $We_{GS} > 0.15$, $We_{LS} < (0.8-0.09P) \exp[(16.15-1.56P)We_{GS}]$, $We_{LS} \leq 2.12 We_{GS}^{-1.04}$ and $We_{LS} \geq 0.0094-We_{GS}^{0.57}$ at elevated pressure ($1.0 \text{ MPa} \leq P \leq 5.0 \text{ MPa}$).
- (d) zone IV: the inertia force of gas dominates, mainly including parallel flow and annular flow, for $We_{LS} < 0.026We_{GS}^{0.86}$ at atmospheric pressure and $We_{LS} < 0.0094We_{GS}^{0.57}$ at elevated pressure.
- (e) zone V: the inertia force of gas and liquid commonly dominate, mainly including churn flow, for $We_{LS} > 0.24We_{GS}^{-0.79}$ at atmospheric pressure and $We_{LS} > 2.12We_{GS}^{-1.04}$ at elevated pressure.

Fig. 14 shows the influence of operating pressure on the gas-liquid two-phase flow pattern map. It can be observed that the transition lines shift to higher We_{GS} and lower We_{LS} at elevated pressure compared to the atmospheric pressure. The transition line, from zone I to II, shifts to higher We_{GS} and lower We_{LS} when the operating pressure increases from 1.0 MPa to 5.0 MPa. Other transition lines from zone II to III, from zone III to IV, and from zone III to V almost remain unchanged at elevated pressure.

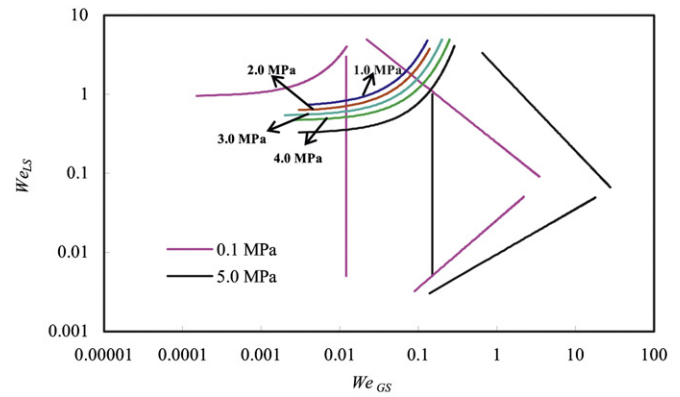


Fig. 14. Flow pattern maps for the present T-junction microchannel based on We_{GS} and We_{LS} at different pressure.

4. Conclusions

Gas-liquid two-phase flow in T-junction rectangular microchannel with the hydraulic diameter of $400 \mu\text{m}$ at atmospheric and elevated pressure ($1.0 \sim 5.0 \text{ MPa}$) has been investigated. The superficial velocities range from 4.62×10^{-2} to 23.15 m/s for gas and from 2.31×10^{-2} to 0.93 m/s for liquid. The gas Weber numbers vary from 1.37×10^{-5} to 3.46 at atmospheric pressure and from 1.70×10^{-3} to 70.32 at elevated pressure, respectively. The effect of operating pressure on the liquid Weber numbers can be ignored, which are in the range of $3.1 \times 10^{-3} \sim 4.9$.

Seven typical flow patterns such as bubbly flow, slug flow, unstable slug flow, parallel flow, slug-annular flow, annular flow and churn flow are also observed in the T-junction rectangular microchannel at atmospheric and elevated pressure, respectively. It is found that the same flow pattern shows different detail characteristics due to the operating pressure, which may induce the different gas-liquid mass transfer and reaction performance.

The hydrodynamic characteristics of gas-liquid two phases are mainly affected by the interfacial tension of gas-liquid two phases, the gas inertia force and the liquid inertia force. Based on the force analysis of gas and liquid in microchannel, the formation mechanism and process of observed flow patterns are discussed at great length. The flow pattern maps are divided into five regions using We_{GS} and We_{LS} as coordinates based on their formation mechanisms. The transition lines shift to higher We_{GS} and lower We_{LS} at elevated pressure compared to the atmospheric pressure. The transition line, from zone I to II, shifts to higher We_{GS} and lower We_{LS} when the operating pressure increases from 1.0 MPa to 5.0 MPa. Other transition lines from zone II to III, from zone III to IV, and from zone III to V almost remain unchanged at elevated pressure.

It is important to note that this study gives a contribution to the influence of operating pressure on the gas-liquid system in T-junction microchannel. This will serve as the basis for future gas-liquid two-phase mass transfer and reaction characteristics in microchannel at elevated pressure.

Nomenclature

A	cross-sectional area of channel, m^2
D_H	hydraulic diameter of microchannel, m
J	superficial velocity, m/s
P	operating pressure, MPa
Q	volumetric flow rate, m^3/s
We	Weber number

Greek symbols

ρ mass density, kg/m³
 σ interfacial tension, N/m

Subscripts

α at atmospheric pressure condition
 G gas phase
 L liquid phase
 r at real operating pressure condition
 S superficial

Acknowledgments

We gratefully acknowledge the financial supports for this project from Ministry of Science and Technology of China (No. 2009CB219903), National Natural Science Foundation of China (Nos. 20911130358, 21106141).

References

- Abdallah, R., Meille, V., Shaw, J., Wenn, D., de Bellefon, C., 2004. Gas–liquid and gas–liquid–solid catalysis in a mesh microreactor. *Chem. Commun.* 4, 372–373.
- Akbar, M.K., Plummer, D.A., Ghiaasiaan, S.M., 2003. On gas–liquid two-phase flow regimes in microchannels. *Int. J. Multiphase Flow* 29, 855–865.
- Anna, S., Bontoux, N., Stone, H.A., 2003. Formation of dispersions using “flow focusing” in microchannels. *Appl. Phys. Lett.* 82, 364–366.
- Baranenkov, V.I., Sysoev, V.S., Falkovskii, L.N., Kirov, V.S., Piontkovskii, A.I., Musienko, A.N., 1990. The solubility of nitrogen in water. *At. Energy* 68, 162–165.
- Chen, J.F., Chen, G.Z., Wang, J.X., Shao, L., Li, P.F., 2011. High-throughput micro-porous tube-in-tube microreactor as novel gas–liquid contactor: mass transfer study. *AIChE J.* 57, 239–249.
- Coleman, J.W., Garimella, S., 1999. Characterization of two-phase flow patterns in small diameter round and rectangular tubes. *Int. J. Heat Mass Trans.* 42, 2869–2881.
- Cubaud, T., Ulmanella, U., Ho, C.M., 2006. Two-phase flow in microchannels with surface modifications. *Fluid. Dyn. Res.* 38, 772–786.
- Deshmukh, S.R., Tonkovich, A.L.Y., Jarosch, K.T., Schrader, L., Fitzgerald, S.P., Kilanowski, D.R., Lerou, J.J., Mazanec, T.J., 2010. Scale-up of microchannel reactors for Fischer-Tropsch synthesis. *Ind. Eng. Chem. Res.* 49, 10883–10888.
- Fu, T.T., Ma, Y.G., Funfschilling, D., Zhu, C.Y., Li, H.Z., 2010. Squeezing-to-dripping transition for bubble formation in a microfluidic T-junction. *Chem. Eng. Sci.* 65, 3739–3748.
- Ganan-Calvo, A., Gordillo, J., 2001. Perfectly monodisperse microbubbling by capillary flow focusing. *Phys. Rev. Lett.* 87, 274501 1–4.
- Garstecki, P., Fuerstman, M.J., Stone, H.A., Whitesides, G.M., 2006. Formation of droplets and bubbles in a microfluidic T-junction—scaling and mechanism of break-up. *Lab. Chip* 6, 437–446.
- Halder, R., Lawal, A., 2007. Experimental studies on hydrogenation of anthraquinone derivative in a microreactor. *Catal. Today* 125, 48–55.
- Jähnisch, K., Hessel, V., Löwe, H., Baerns, M., 2004. Chemistry in microstructured reactors. *Angew. Chem. Int. Ed.* 43, 406–446.
- Kashid, M.N., Renken, A., Kiwi-Minsker, L., 2011. Gas–liquid and liquid–liquid mass transfer in microstructured reactors. *Chem. Eng. Sci.* 66, 3876–3897.
- Kawahara, A., Chung, P.M.Y., Kawaji, M., 2002. Investigation of two-phase flow pattern, void fraction and pressure drop in a microchannel. *Int. J. Multiphase Flow* 28, 1411–1435.
- Kawahara, A., Sadatomi, M., Nei, K., Matsuo, H., 2011. Characteristics of two-phase flows in a rectangular microchannel with a T-junction type gas–liquid mixer. *Heat Transfer Eng.* 32, 585–594.
- Kockmann, N., 2007. *Transport Phenomena in Micro Process Engineering*. Springer.
- Kreutzer, M.T., Kapteijn, F., Moulijn, J.A., Kleijn, C.R., Heiszwolf, J.J., 2005. Inertial and interfacial effects on pressure drop of Taylor flow in capillaries. *AIChE J.* 51, 2428–2440.
- Leclerc, A., Alamé, M., Schweich, D., Pouteau, P., Delattre, C., de Bellefon, C., 2008. Gas–liquid selective oxidations with oxygen under explosive conditions in a micro-structured reactor. *Lab. Chip* 8, 814–817.
- Letzel, H.M., Schouten, J.C., Krishna, R., van den Bleek, C.M., 1999. Gas holdup and mass transfer in bubble column reactors operated at elevated pressure. *Chem. Eng. Sci.* 54, 2237–2246.
- de Menech, M., Garstecki, P., Jousse, F., Stone, H.A., 2008. Transition from squeezing to dripping in a microfluidic T-shaped junction. *J. Fluid Mech.* 595, 141–161.
- Mills, P.L., Chaudhari, R.V., 1997. Multiphase catalytic reactor engineering and design for pharmaceuticals and fine chemicals. *Catal. Today* 37, 367–404.
- Qian, D.Y., Lawal, A., 2006. Numerical study on gas and liquid slugs for Taylor flow in a T-junction microchannel. *Chem. Eng. Sci.* 61, 7609–7625.
- Shao, N., Gavriilidis, A., Angeli, P., 2009. Flow regimes for adiabatic gas–liquid flow in microchannels. *Int. J. Multiphase Flow*. 64, 2749–2761.
- Shao, N., Gavriilidis, A., Angeli, P., 2011. Effect of inlet conditions on Taylor bubble length in microchannels. *Heat Transfer Eng.* 32, 1117–1125.
- Stanley, R.S., Barron, R.F., Ameal, T.A., 1997. Two-phase flow in microchannels. *Micro-Electro-Mechanical Systems (MEMS)*. ASME DSC-vol. 62/HTD-vol.354.
- Tadepalli, S., Halder, R., Lawal, A., 2007. Catalytic hydrogenation of o-nitroanisole in a microreactor: reactor performance and kinetic studies. *Chem. Eng. Sci.* 62, 2663–2678.
- Trachsel, F., Hutter, C., von Rohr, P.R., 2008. Transparent silicon/glass microreactor for high-pressure and high-temperature reactions. *Chem. Eng. J.* 135 S, S309–S316.
- Triplett, K.A., Ghiaasiaan, S.M., Abdel-Khalik, S.I., Sadowski, D.L., 1999. Gas–liquid two-phase flow in microchannels Part I: two-phase flow patterns. *Int. J. Multiphase Flow* 25, 377–394.
- Waelchli, S., von Rohr, P.R., 2006. Two-phase flow characteristics in gas–liquid microreactors. *Int. J. Multiphase Flow* 32, 791–806.
- Wiegand, G., Franck, E.U., 1994. Interfacial tension between water and non-polar fluids up to 473 K and 2800 bar. *Ber. Bunsen-Ges. Phys. Chem. Chem. Phys.* 98, 809–817.
- Xu, J.H., Li, S.W., Chen, G.G., Luo, G.S., 2006. Formation of monodisperse micro-bubbles in a microfluidic device. *AIChE J.* 52, 2254–2259.
- Ye, C.B., Chen, G.W., Yuan, Q., 2012. Process characteristics of CO₂ absorption by aqueous monoethanolamine in a microchannel reactor. *Chin. J. Chem. Eng.* 20, 111–119.
- Yeong, K.K., Gavriilidis, A., Zapf, R., Hessel, V., 2004. Experimental studies of nitrobenzene hydrogenation in a microstructured falling film reactor. *Chem. Eng. Sci.* 59, 3491–3494.
- Yue, J., Chen, G.W., Yuan, Q., Luo, L.A., Gonthier, Y., 2007. Hydrodynamics and mass transfer characteristics in gas–liquid flow through a rectangular microchannel. *Chem. Eng. Sci.* 62, 2096–2108.
- Yue, J., Luo, L.A., Gonthier, Y., Chen, G.W., Yuan, Q., 2008. An experimental investigation of gas–liquid two-phase flow in single microchannel contactors. *Chem. Eng. Sci.* 63, 4189–4202.
- Yue, J., Luo, L.A., Gonthier, Y., Chen, G.W., Yuan, Q., 2009. An experimental study of air–water Taylor flow and mass transfer inside square microchannels. *Chem. Eng. Sci.* 64, 3697–3708.
- Zhao, T.S., Bi, Q.C., 2001. Co-current air–water two-phase flow patterns in vertical triangular microchannels. *Int. J. Multiphase Flow* 27, 765–782.
- Zhao, Y.C., Chen, G.W., Yuan, Q., 2006. Liquid–liquid two-phase flow patterns in a rectangular microchannel. *AIChE J.* 52, 4052–4060.
- Zhao, Y.C., Chen, G.W., Yuan, Q., 2007. Liquid–liquid two-phase mass transfer in the T-junction microchannels. *AIChE J.* 53, 3042–3053.